Monthly Notices
of the
ROYAL ASTRONOMICAL SOCIETY

Mon. Not. R. Astron. Soc. **427,** 2701–2710 (2012) doi:10.1111/j.1365-2966.2012.21248.x

Composite reverberation mapping

S. Fine,[1,2]★ T. Shanks,[1] S. M. Croom,[3] P. Green,[4] B. C. Kelly,[4] E. Berger,[4] R. Chornock,[4] W. S. Burgett,[5] E. A. Magnier[5] and P. A. Price[6]

[1]*Department of Physics, Durham University, South Road, Durham DH1 3LE*
[2]*Department of Physics, University of Western Cape, Bellville 7535, Cape Town, South Africa*
[3]*Sydney Institute for Astronomy, School of Physics, The University of Sydney, NSW 2006, Australia*
[4]*Harvard–Smithsonian Center for Astrophysics, 60 Garden Street, Cambridge, MA 02138, USA*
[5]*Institute for Astronomy, University of Hawaii at Manoa, Honolulu, HI 96822, USA*
[6]*Department of Astrophysical Sciences, Princeton University, Princeton, NJ 08544, USA*

Accepted 2012 May 3. Received 2012 April 2; in original form 2012 February 20

ABSTRACT

Reverberation mapping offers one of the best techniques for studying the inner regions of quasi-stellar objects (QSOs). It is based on cross-correlating continuum and emission-line light curves. New time-resolved optical surveys will produce well-sampled light curves for many thousands of QSOs. We explore the potential of stacking samples to produce composite cross-correlations for groups of objects that have well-sampled continuum light curves, but only a few (∼2) emission-line measurements. This technique exploits current and future wide-field optical monitoring surveys [e.g. Pan-STARRS, Large Synoptic Survey Telescope (LSST)] and the multiplexing capability of multi-object spectrographs (e.g. 2dF, Hectospec) to significantly reduce the observational expense of reverberation mapping, in particular at high redshift (0.5–2.5).

We demonstrate the technique using simulated QSO light curves and explore the biases involved when stacking cross-correlations in some simplified situations. We show that stacked cross-correlations have smaller amplitude peaks compared to well-sampled correlation functions as the mean flux of the emission light curve is poorly constrained. However, the position of the peak remains intact. We find that there can be 'kinks' in stacked correlation functions due to different measurements contributing to different parts of the correlation function. While the magnitude of the kinks must be fitted for, their positions and relative strengths are known from the spectroscopic sampling distribution of the QSOs making the bias a one-parameter effect. We also find that the signal-to-noise ratio in the correlation functions for the stacked and well-sampled cases is comparable for the same number of continuum and emission-line measurement pairs.

Using the Pan-STARRS Medium-Deep Survey (MDS) as a template, we show that cross-correlation lags should be measurable in a sample size of 500 QSOs that have weekly photometric monitoring and two spectroscopic observations. Finally, we apply the technique to a small sample (42) of QSOs that have light curves from the MDS. We find no indication of a peak in the stacked cross-correlation. A larger spectroscopic sample is required to produce robust reverberation lags.

Key words: galaxies: active – galaxies: nuclei – quasars: emission lines – quasars: general – galaxies: Seyfert.

1 INTRODUCTION

The inner regions of active galactic nuclei (AGN) offer a unique opportunity to study matter within a few parsecs of a supermassive black hole. Reverberation mapping is designed to study (primarily) the broad-line region (BLR) of AGN by measuring the interaction between continuum and broad-line flux variations (Blandford & McKee 1982; Peterson 1993). The physical model assumes that the BLR is photoionized by an ultraviolet (UV) continuum that is emitted from a much smaller radius. Variations in the ionizing continuum produce equivalent variations in the broad emission-line flux after a delay that can be associated with the light travel time.

★E-mail: stephen.fine@durham.ac.uk

Reverberation mapping of a single system requires many epochs of emission-line and continuum luminosity measures. A peak in the cross-correlation between the two light curves indicates the time lag between continuum and emission-line variations. To date lags have been measured for some tens of objects following this approach (Peterson et al. 2004; Bentz et al. 2006, 2010; Denney et al. 2006, 2010).

Reverberation mapping has led to significant advances in the understanding of AGN [the radius–luminosity relation (Wandel, Peterson & Malkan 1999; Kaspi et al. 2000), stratification and kinematics of the BLR (Peterson & Wandel 1999, 2000), black hole mass estimates (Peterson et al. 2004), etc.]. However, these campaigns are observationally expensive and time consuming as they require many observations of individual objects over a long period of time.

Rather than focusing on obtaining many hundreds of epochs of observations on single objects, this paper explores an observational technique that is only now becoming possible due to the new generation of time-resolved photometric surveys and the multiplexing capabilities of multiple-object spectrographs (MOSs).

Time-resolved surveys, such as those being performed with the Pan-STARRS1 (PS1) telescope (Kaiser et al. 2002), will measure the broad-band (continuum) light curves of many thousands of quasi-stellar objects (QSOs). The PS1 Medium-Deep Survey (MDS) is taking images of ten 7-deg^2 fields every few days in five photometric bands. Number counts imply that there are $\sim$500 QSOs with $g < 22$ in each of these fields (Croom et al. 2009) making them easily surveyable with current MOSs in $\sim$1 night of observing time. Repeating the spectroscopic observations regularly would allow traditional reverberation mapping to be performed on samples of thousands of QSOs. However, this would require a large amount of observing time on highly subscribed telescopes to produce results. In this paper we look at the potential for reverberation mapping in stacked samples of QSOs that only have a few ($\sim$2) spectroscopic epochs of data, but are coupled with well-sampled continuum light curves.

In Section 2 we outline the principle of stacking cross-correlations, then in Section 3 we simulate QSO light curves to illustrate the technique, in Section 4 we present an empirical simulation of a QSO survey and the potential results, in Section 5 we apply the technique to early data from a spectroscopic survey of QSOs in the MDS region and in Section 6 we summarize the results of our investigation. Throughout this paper we use a flat $(\Omega_{\rm m}, \Omega_\Lambda) = (0.3, 0.7)$, $H_0 = 70\,{\rm km\,s^{-1}\,Mpc^{-1}}$ cosmology.

2 OUTLINE OF APPROACH

Observed light curves are made up of a series of (often unevenly sampled) discrete measurements. Estimates of the cross-correlation between continuum and emission-line light curves (denoted C and L below) are therefore limited by their sampling. A variety of techniques have been developed for estimating cross-correlations with observational samples (Gaskell & Sparke 1986; Gaskell & Peterson 1987; Zu, Kochanek & Peterson 2011). In this paper, we will focus on the discrete cross-covariance function (Edelson & Krolik 1988) as it lends itself simply to the stacking technique. The discrete cross-covariance is calculated in terms of pairs of observations (C_i, L_j). Taking all pairs of continuum and emission-line observations such that the time lag $t_i - t_j$ is between τ and $\tau + \delta\tau$, the cross-covariance amplitude for lag τ is estimated with

$$X(\tau) = \sum_{i,j}^{t_i - t_j \in [\tau, \tau+\delta\tau]} \frac{(C_i - \overline{C})(L_j - \overline{L})}{n_{\rm pair}}, \quad (1)$$

where $n_{\rm C}$ and $n_{\rm L}$ are the number of continuum and emission-line measurements, respectively. $\delta\tau$ defines the bin size in the cross-correlation. Here we will use fixed bin sizes, but see Alexander (1997) for the use of variable bin sizes to optimize results. Equation (1) is the same as that for the cross-correlation except that it is not normalized by the rms of each variable. $\delta\tau$ defines the bin size in the cross-correlation. In this paper, we will focus on the covariance rather than the correlation function as they are almost equivalent in terms of the analysis presented here but using the cross-covariance clarifies the discussion in later sections.

The discrete cross-covariance is a function on pairs of observations. Assuming all measurements have the same errors and well-defined mean levels, the variance of the cross-covariance is inversely proportional to the number of data–data pairs. Therefore, desirable results require a large number of pairs of observations at a wide range of time lags. Traditionally, this is achieved through repeat observations of an object over a period of years to build up sufficient data at all time lags. However, there is no explicit reason that all of the data must come from a single source. Given a group of objects that have similar variability properties, we are able to combine the data–data pairs from each object in the group to obtain a 'composite' cross-covariance function with higher signal-to-noise ratio (S/N) than is obtainable for the individual objects. Essentially, this process is the same as calculating the covariance function for each object and then stacking them.

This stacking technique has been used before for continuum autocovariance/autocorrelation analysis (Almaini et al. 2000; Vanden Berk et al. 2004; Wilhite et al. 2007), but to our knowledge it has not previously been applied to cross-covariances and/or reverberation mapping.

3 SIMULATING DATA

To demonstrate the principle of stacking cross-covariances, we simulate QSO continuum and emission-line light curves. We model the continuum as a first-order autoregressive process following e.g. Kelly, Bechtold & Siemiginowska (2009), MacLeod et al. (2010) and Zu et al. (2012). Simulating this process requires a damping time-scale $\tau_{\rm c}$ and amplitude of short-time-scale variations $\sigma_{\rm c}$ that we fix for each simulation.

The emission-line flux at a given time is defined by convolving the continuum light curve with a given transfer function that is a function of τ (e.g. Edelson & Krolik 1988). The transfer function is not well constrained observationally for AGN. For simplicity, we use a Gaussian with unit area centred on $\tau = \tau_{\rm l}$ with full width at half-maximum $\tau_{\rm l}/2$. Note that this is not a physically motivated transfer function, but is roughly similar to empirical transfer functions for Balmer lines that have been reverberation mapped (Horne, Welsh & Peterson 1991; Bentz et al. 2010).

After simulating the light curves, we add random Gaussian noise into the continuum and emission-line data with rms $e_{\rm c}$ and $e_{\rm l}$ to simulate uncorrelated effects and measurement error.

In total there are five input parameters. For each set of simulations we perform, we will create many light curves. Each time we simulate a light curve, we draw the input parameters from Gaussian distributions with a mean and rms fixed for that set of simulations and Table 1 gives a list of these parameters.

Table 1. Parameters used when simulating light curves (see text for the definitions of each parameter). In each case, the parameter used in a simulation is drawn from a Gaussian distribution with mean and rms given in this table. Parameters that are required to be positive have their distribution functions truncated at zero.

Parameter	σ_c (flux)	τ_c (d)	τ_l (d)	e_c (flux)	e_l (flux)
Mean	5.0	20.0	40.0	0.2	0.2
rms	1.0	5.0	5.0, 30.0	0.1	0.1

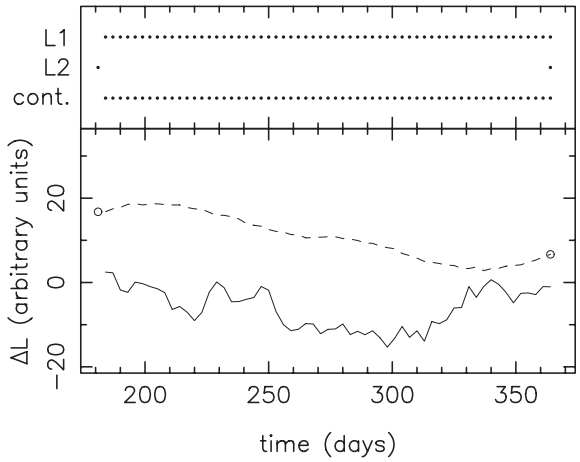

Figure 1. Bottom: example of a simulated continuum (solid) and emission-line (dashed) light curve. The dashed curve has been offset from the solid for clarity. The dots in the top panel show how the continuum and emission line are sampled in the case of L1 and L2.

3.1 Stacked versus non-stacked cross-covariance functions

To demonstrate the principle of stacking cross-covariances we will concentrate on two simplified scenarios. In each scenario, we assume that a QSO is observed photometrically (giving us continuum luminosity measures) every three days for six months of the year. In the first case (L1), we assume that at every date we get photometric data we also obtain a spectrum and emission-line flux measure. In the second case (L2), we only obtain line fluxes twice a year at either end of the continuum sampling. The L1 scenario is designed to be equivalent to standard reverberation mapping with large numbers of emission-line and continuum measurements, while L2 demonstrates the stacking technique. We illustrate these situations in Fig. 1. The top panel in the figure shows the sampling over six months of the continuum and emission line in each of the cases. Below we show a simulated light curve of the continuum (solid line) and the emission line (dashed line) over the period (solid line) using the parameters from Table 1.

If we take just a single year's worth of data, there are 61 continuum measurements and 61 and two emission-line measurements for L1 and L2, respectively. In the case of L1, we create 1000 simulated continuum and emission-line light curves. We calculate the cross-covariance function in each case and in Fig. 2(a) we plot the average of the 1000 covariance functions along with the rms between simulations as error bars.

Since there are ∼30 times the number of spectroscopic measurements in L1, we compare this with a case where 30 QSOs have been sampled as in L2. The cross-covariances from the 30 QSOs are then stacked to produce an ensemble covariance function. We simulate this situation 1000 times and plot the results in Figs 2(b) and (c), the difference between these simulations is that the first has the rms of $\tau_l = 5.0$ days, while the second has $\tau_l = 30.0$ days to illustrate the effect of increasing the scatter in reverberation lags.

It is apparent that, in our simulations at least, we can reproduce the peak in the cross-covariance function at $\tau_l = 40$ using stacked covariance functions. However, there are differences between the cross-covariances for L1 and L2. In the following subsections, we discuss the most prominent of these.

3.1.1 Peak height in stacked versus non-stacked cross-covariances

The peak in the covariance function for L2 is biased low because we are undersampling the emission-line light curve and so are unable to define the mean level precisely. The value of $\overline{L}$ in equation (1) is heavily biased by the two individual measurements of L_i, hence the covariance function is weaker. We can derive the expected level of this bias in the case of n_L measurements of the emission-line luminosity. Taking the definition of the discrete cross-covariance:

$$\begin{aligned} X(\tau) &= \sum \frac{(C_i - \overline{C})\left(L_j - \frac{\sum L_k}{n_L}\right)}{n_{\rm pair}} \\ &= \sum \frac{(C_i - \overline{C})\left(L_j - \frac{L_j}{n_L} - \frac{\sum_{k\neq j} L_k}{n_L}\right)}{n_{\rm pair}} \\ &= \sum \frac{\frac{n_L-1}{n_L}(C_i - \overline{C})(L_j - \overline{L}_{k\neq j})}{n_{\rm pair}} \end{aligned} \qquad (2)$$

(note that the sums here are over the same data points as equation 1) $\overline{L}$ in equation (2) is now calculated over the $n_L - 1$ emission-line measurements not including L_j and so is unbiased by L_j. Hence the amplitude of a cross-covariance calculated from n_L emission-line measurements will be proportional to $(n_L - 1)/n_L$. This is nearly a factor of 2 in the case of L1 compared to L2 in our simulations as is illustrated in Fig. 2.

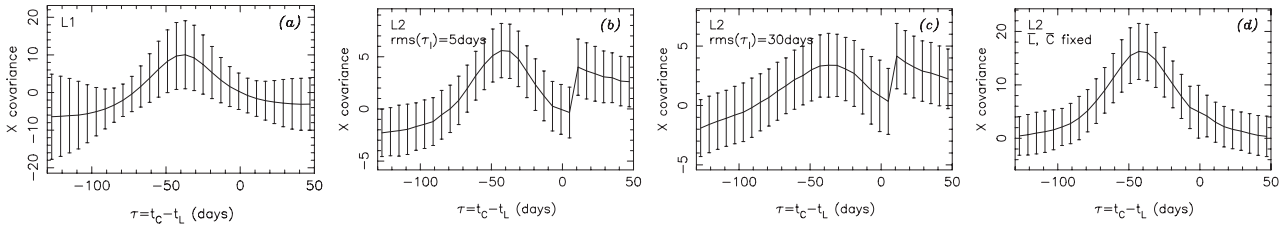

Figure 2. Comparison between the mean cross-covariance functions for a single QSO with 61 epochs of spectroscopic data (L1; a) and 30 QSOs with only two epochs (L2; b). (c) shows the same simulations as (b) except the distribution of lags used is 40 ± 30 days rather than ± 5. In (d) the L2 simulation is rerun with rms(τ_l) = ± 5.0, but the cross-covariance functions are calculated using the known values of $\overline{L}$ and $\overline{C}$ rather than calculating them from the simulated observations.

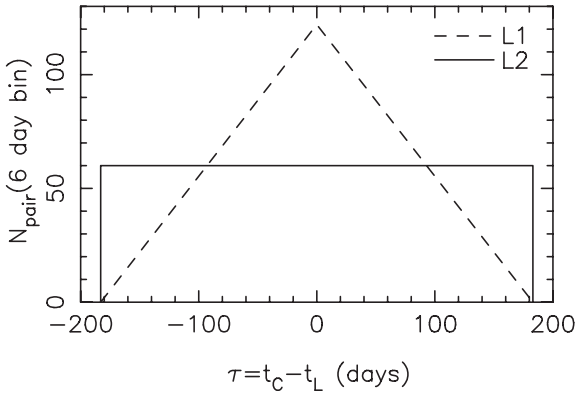

Figure 3. The number of emission-line and continuum data–data pairs that are used in the cross-covariance calculation. We compare the L1 and L2 examples (see the text) with a bin size of six days.

Note that had we calculated cross-correlation rather than covariances this effect is not as important since the rms of the L_i values (that normalizes a cross-correlation) is affected in the same manner as the covariance.

3.1.2 Errors in stacked versus non-stacked cross-covariances

The rms error bars on the L1 cross-covariance are not all equal and decrease from left to right. In the case of L2 the error bars are roughly constant. The different ways that the emission-line light curves are sampled for L1 and L2 mean that the number of data–data pairs contributing to the covariance function at a given τ is not the same in each case.

In Fig. 3 we plot the number of data–data pairs contributing to a covariance function as a function of τ for L1 and L2. The constant time sampling of L1 leads to a more concentrated distribution of lags. In the case of L2 the distribution is flat while the total number of pairs is approximately the same for L1 and L2. This leads to an increase in the noise of L1 cross-covariances in the undersampled areas of lag space around six months.

In general, the errors are considerably larger in the case of L1 compared to L2. This is because L1 oversamples the light curve we have simulated and, while the number of measurements going into the L1 and the stacked L2 cross-covariances is roughly the same, the emission-line measurements are correlated in the case of L1, increasing the noise.

3.1.3 The 'kink' in the L2 cross-covariance

The 'kink' in the L2 cross-covariance occurs because we have only two measurements of the emission-line luminosity, and because the mean of the continuum level is not accurately defined.

At any lag in an individual cross-covariance for L2 (before stacking) there is only one data–data pair available to define the cross-covariance. All of the positive lags use the first line measurement, and all of the negative lags use the second. The kink in Fig. 2(b) occurs as we move from one regime to the other. To explain the kink we take the definition of the discrete cross-covariance in the case of just two line measurements:

$$X(\tau) = \sum \frac{(C_i - \overline{C})(L_j - \overline{L})}{n_{\rm pair}} = (C_i - \overline{C})[L_j - (L_1 + L_2)/2] \quad (3)$$

since there are only two emission-line measurements and only one continuum–line pair contributes at a given lag. If we use $L_{j'}$ to denote the emission-line measurement that is not L_j, then

$$X(\tau) = 0.5(C_i - \overline{C})(L_j - L_{j'}). \quad (4)$$

We now calculate the expectation value of the cross-covariance. We use angled brackets to denote the expectation value that is averaged over a large number of realizations; this is distinct from the average of the individual continuum luminosities ($\overline{C}$), which is calculated over the number of observations of a single object:

$$\langle X(\tau)\rangle = 0.5(\langle C_i L_j\rangle - \langle C_i L_{j'}\rangle - \langle \overline{C} L_j\rangle + \langle \overline{C} L_{j'}\rangle).$$

We notate the covariance of two variables as $\mathrm{cov}(x, y) = \langle xy\rangle - \langle x\rangle\langle y\rangle$:

$$\begin{aligned}\langle X(\tau)\rangle &= 0.5[\langle C_i\rangle\langle L_j\rangle + \mathrm{cov}(C_i, L_j) - \langle C_i\rangle\langle L_{j'}\rangle - \mathrm{cov}(C_i, L_{j'}) \\ &\quad - \langle\overline{C}\rangle\langle L_j\rangle - \mathrm{cov}(\overline{C}, L_j) + \langle\overline{C}\rangle\langle L_{j'}\rangle + \mathrm{cov}(\overline{C}, L_{j'})] \\ &= 0.5[\mathrm{cov}(C_i, L_j) - \mathrm{cov}(C_i, L_{j'}) - \mathrm{cov}(\overline{C}, L_j) + \mathrm{cov}(\overline{C}, L_{j'})]. \end{aligned} \quad (5)$$

The first term of equation (5) is the quantity we are trying to measure with the cross-covariance. The other terms are biases. The factor of 0.5 is due to there only being two emission-line measurements (see Section 3.1.1). For the second term note that $\mathrm{cov}(C_i, L_1) < \mathrm{cov}(C_i, L_2)$. However, this term will be small with respect to the other biases. For the other terms, $\mathrm{cov}(\overline{C}, L_1)$ will be small as $\overline{C}$ is calculated from the continuum light curve that is measured after L_1 while L_1 is dependent on the continuum level before it is measured. $\mathrm{cov}(\overline{C}, L_2)$ on the other hand is significant. This is partly due to the manner in which we have constructed our simulation. The autoregressive continuum light curve means that continuum points are covariant with their neighbours, as we may expect is the case in reality. Furthermore, the transfer function that is used to define the emission-line luminosity makes L_2 covariant with a number of the continuum points.

Given the values in Table 1, we can calculate $\mathrm{cov}(\overline{C}, L_1)$, $\mathrm{cov}(\overline{C}, L_2)$, $\mathrm{cov}(C_1, L_2)$ and $\mathrm{cov}(C_{n_C}, L_1)$ to get the expected offset in the cross-covariance between $\tau < 0$ and $\tau > 0$. These are, respectively, 0.43, 5.04, 0.03 and 0.0004 in the units used. Hence we expect the offset to be ∼4.6 in Fig. 2(b). This is in good agreement with our simulations.

In Fig. 2(d) we reproduce the simulations in (b), except that rather than calculating $\overline{C}$ and $\overline{L}$ from the simulated light curves, we use their correct values as defined in the simulation. In this case, the bias is not apparent and there is no kink in the covariance function.

3.2 Optimizing the stacked results

The major source of bias in the stacked covariance functions is the poorly defined mean levels, particularly $\overline{L}$. The precision of $\overline{C}$ can be improved simply with more measurements and, in the practical example we give below of the Pan-STARRS survey there will eventually be many more than the ∼60 photometric measurements that we have assumed here.

While more spectroscopic measurements would increase the precision of $\overline{L}$, this somewhat goes against the principle of the technique. Less biased values for $\overline{L}$ can be estimated from $\overline{C}$ and the global equivalent width distribution at fixed luminosity. However, this would also include a significant loss of precision and would smooth the kink in the correlation function at the expense of S/N. Since the time sampling of the continuum and emission line is known, the location of the kink and the shape (if not magnitude) of

its effect on the covariance function can be estimated. Removing the bias from the results then requires a one-parameter fit to the data. In this case the magnitude of the bias can hold important information on the covariances between emission line and continuum emission in QSOs and, accurately measured, could help studies of transfer functions and the interactions between the accretion disc and BLR.

The distribution of the reverberation lags of the quasars that are stacked in this manner has the effect of smoothing out the stacked covariance function. This broadens the peak in the stacked covariance function and hence reduces the signal in the peak. The two values of rms($\tau_{\rm l}$) used in the above simulations are used to illustrate this effect with extreme values. The lack of large numbers of objects that have several reverberation mapped lines means that we cannot be certain of the distribution of lags for high-redshift quasars. However, the Hβ line has been mapped for a significant number of Seyferts. While there has been a considerable range of lags measured, almost all of this variation has been shown to be due to the radius–luminosity relation. Kaspi et al. (2005) find only ∼15 per cent intrinsic scatter around this relation. Furthermore, the small degree of scatter in Mg II and C IV line widths for the brightest quasars may indicate that there is even less intrinsic scatter in the radius–luminosity relation in that regime (Fine et al. 2008, 2010). Hence it would be advisable to use quasars with a small range of luminosities when calculating a stacked cross-covariance to improve the signal. Indeed this may be advisable anyway since one of the primary applications of this technique would be to evaluate the radius–luminosity relation for UV quasar lines.

To get a better idea of what results we may expect from a feasible survey of quasars, we design a simulation based on what is currently known about AGN. In the next section, we present this simulation to give a realistic impression of the results that could be achieved with this technique.

4 A PHYSICALLY MOTIVATED SIMULATION FOR STACKED REVERBERATION MAPPING WITH THE Pan-STARRS MDS

In the remainder of this paper, we make a preliminary application of the method in the Pan-STARRS MDS. The MDS consists of ten 7-deg^2 fields that are imaged every few nights in five photometric bands ($g_{\rm P1}r_{\rm P1}i_{\rm P1}z_{\rm P1}y_{\rm P1}$). The size of the fields, along with QSO number counts, make each field surveyable with the current generation of multi-object spectrographs in ∼1 night of observing time, yielding ∼500 QSOs (with $g_{\rm P1} < 22$). The regular photometric monitoring of the fields means that for every spectrum taken there are many continuum–emission-line data pairs that can be used in cross-covariance analyses.

To evaluate the potential for reverberation mapping in the MDS fields, we run simulations based on current knowledge of QSO variability parameters. We assume that a QSO survey is performed similar to the 2SLAQ QSO survey (Croom et al. 2009) and simulate a single MDS field of data with the following prescription.

(i) From 2SLAQ number counts we assume 500 QSOs total. We therefore draw 500 QSOs at random from the 2SLAQ catalogue but only accept those objects at the right redshift to have Mg II in an optical spectrum ($0.4 < z < 2.4$).

(ii) For each object we use the BH mass estimates in Fine et al. (2008) and scaling relations from MacLeod et al. (2010) to obtain the continuum variability parameters $\sigma_{\rm C}$ and $\tau_{\rm C}$ in the observed $g_{\rm P1}$ band assuming 0.3- and 0.15-dex scatter about the mean relations, respectively.

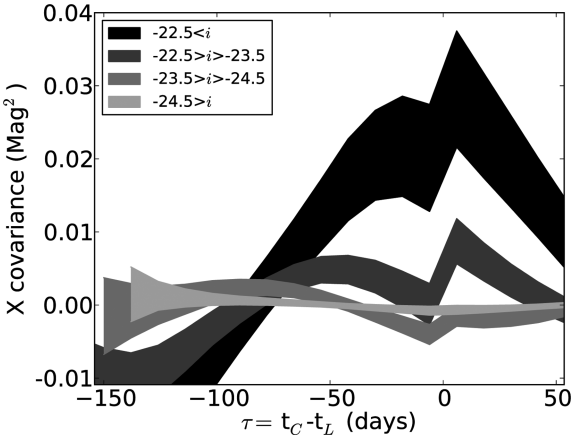

Figure 4. Simulated cross-covariance functions between Mg II emission-line and $g_{\rm P1}$-band light curves for a survey of an MDS field. We assumed that there would be 500 objects in the field and simulated individual QSO parameters by drawing randomly from the 2SLAQ catalogue. The objects are split into four bins by absolute magnitude to show the tendency towards longer lags in brighter objects.

(iii) We extrapolate from the i-band magnitude to 5100 Å assuming a power-law continuum of $f_\lambda \propto \lambda^{-1.5}$ and use the radius–luminosity relation from Kaspi et al. (2005) with 0.1-dex scatter to obtain the lag for the emission-line response $\tau_{\rm L}$ under the assumption that the Mg II and Hβ lines have similar lags (McLure & Jarvis 2002).

(iv) Time-scales are converted to the observed frame and continuum light curves are simulated assuming six-day sampling over an eight-month period. Emission-line flux values are calculated as previously with one spectrum at the beginning and end of the continuum points.

(v) We then add random scatter to the continuum points based on the error on the 2SLAQ magnitude and add 10 per cent scatter to the emission-line points to simulate measurement errors.

In Fig. 4 we bin eight months worth of data by the $i_{\rm P1}$-band absolute magnitude and plot the stacked cross-covariances. The shaded areas show the regions within the rms of the mean cross-correlation when using 12-day bins in the discrete cross-covariance. The figure shows that the tendency towards longer lags in brighter QSOs may be detectable in a single year's worth of data on a single MDS field given the above assumptions.

For each individual realization in our simulations we try to find the peak in the cross-covariance functions. We fit a Gaussian, plus an offset, plus a step at $\tau = 0$ days. The step function corrects for the kink in the covariance functions at $\tau = 0$ days. In Fig. 5 we show the simulated cross-covariance for a single magnitude bin in one of our realizations along with the fitted Gaussian+step.

Using the fit Gaussians we find the location of the peak in the cross-correlations. The distributions of these values are shown in Fig. 6 for each of the magnitude bins. Note that we do not constrain any of the parameters in the fits but still find a peak in the range of time-scales sampled for almost all (>99 per cent) of the realizations except in the brightest magnitude bin. In the brightest bin the time-scales are longer and we only obtain a lag in ∼40 per cent of the realizations. Note that in some cases a Gaussian gives a poor automated fit to the cross-covariance. More careful fitting in individual cases would give better results. The mean $\tau_{\rm L}$ values in the simulated light curves are 27, 54, 97 and 227 days for the faintest to brightest magnitude bins. The fact that we measure

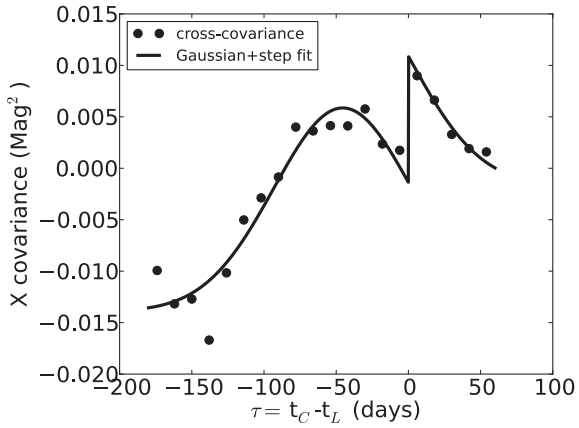

Figure 5. Simulated cross-covariance function for a single magnitude bin in one of our simulations (points) and the functional fit to it (solid line). Here, a Gaussian fits the simulated points and the kink at $\tau = 0$ days is corrected by the step function.

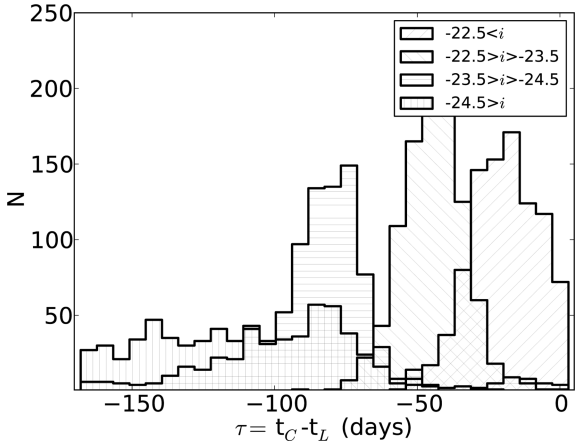

Figure 6. The distribution of the peaks in individual simulated cross-covariances, binned by $i_{\rm P1}$-band magnitude, as defined by Gaussian fits. The tendency for longer lags in the brighter bins is clear here. The brightest bin has lags that are too long to be properly sampled and we only find a good peak in ∼40 per cent of the simulations.

considerably smaller lags than this is due to the fainter objects in each bin being more variable and hence contributing more to the stacked correlation function.

4.1 The potential of stacked cross-covariance functions

We have demonstrated that, at least in our simulations, it is possible to retrieve an average radius–luminosity relation for a sample of quasars. If possible this would be of considerable interest for quasar studies. The radius–luminosity relation has not been strongly constrained for any emission lines other than Hβ. However, UV lines (notably Mg II and C IV) are commonly used to estimate virial black hole masses in high-redshift quasars (e.g. McLure & Jarvis 2002; Vestergaard 2002). These virial mass estimates are based on the assumption that a radius–luminosity relationship exists for these UV lines equivalent to that measured for Hβ. An observational determination of these relations, even if only in averaged stacks, would be of great use in determining black hole masses in high-redshift quasars.

The simulations performed in Section 4 assumed a parent sample of 500 quasars. The MDS survey as a whole would contain ∼5000 quasars to the flux limit we assume. It is not beyond the scope of current telescopes to survey this number of objects nearly twice yearly. Such a data set, in particular if built up over several years, would offer the potential to make extremely high-precision stacked covariance functions. These could offer a unique opportunity to study the transfer function and hence the structure of the BLR although such studies would have to be mindful that convolved into the covariance function is the distribution of different lags and transfer functions of the different quasars in a stack.

Multiple lines could be mapped for the same stacks of quasars. These data give relative information on the stratification of the BLR and where the various emission zones are in quasars. Combined with dynamical measurements (i.e. line profiles) these give indications of the dominant motions in the BLR.

The potential gains from being able to reverberation-map high-z quasars are significant. Above we have outlined just a few. This paper presents a technique that we believe offers a feasible rout towards obtaining these results.

Recent studies have also suggested either narrow- or broad-band 'photometric' reverberation mapping as an observationally cheaper method for obtaining reverberation lags for quasars (e.g. Cherepashchuk & Lyutyi 1973; Haas et al. 2011; Chelouche & Daniel 2012). While neither technique has been proven for large-scale samples the relative gains of each technique are somewhat unclear. Narrow-band photometric mapping requires that the quasars are at the correct redshift for the filter, and so cannot be applied on such large scales as the other two methods. Broad-band photometric reverberation mapping is more efficient than the technique described here in terms of the spectroscopy required. However, a single epoch of spectroscopy is required to obtain accurate redshifts. The complexity of decoupling continuum and emission-line light curves and the effects of having several lines in a single filter requires extremely accurate photometry and complex reduction techniques. On the other hand, broad-band photometric reverberation mapping does not require the complexity of obtaining flux-calibrated fibre spectra with high enough S/N to calculate precise line fluxes. Finally, a major gain for stacked covariance functions is the flat sampling distribution (Fig. 3). Bright quasars can have continuum time-scales of years, and correspondingly large BLR lags. Obtaining good constraints on these lags requires sampling many times the continuum+lag time-scale in classical reverberation mapping. However, in our technique one needs only sample $1 \times$ the continuum+lag time-scale and then information is built up through stacking.

The problem of obtaining robust reverberation mapping results in the high-redshift Universe is a problem that may be solved with current and planned time-resolved photometric surveys. In the rest of the paper we apply our technique to a small number of objects that already have the correct observations available.

5 Pan-STARRS MDS EARLY DATA

In this section we derive MDS light curves for a sample of QSOs that have >1 spectra, and calculate the stacked cross-covariance function for the sample.

5.1 PS1 light curves

The PS1 telescope (Hodapp et al. 2004) is performing a series of time-resolved photometric surveys of the northern sky. We are

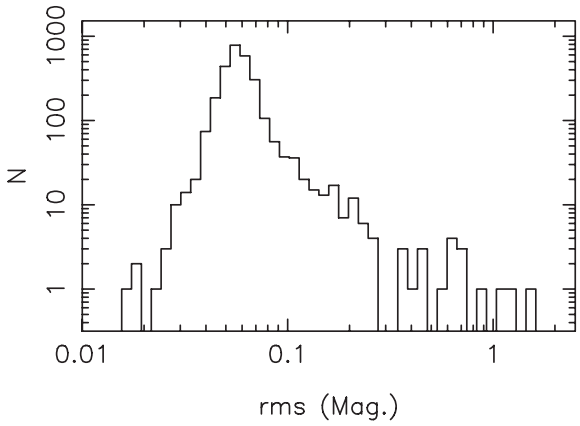

Figure 7. The rms of the calibration offset between PS1 g_{P1}-band and SDSS g-band photometry in the MD03 field. In cases where the rms is >0.1 mag, the calibration is deemed to be suspect and the skycell is rejected. This corresponds to ∼5 per cent of the individual skycells.

particularly interested in the MDS as offering the best opportunity for our analysis. Images of the 10 MDS fields are taken every four to five nights in each of the photometric bands while not affected by the Sun or Moon. On each night, eight dithered exposures are taken and combined to form a nightly stack (see e.g. Kaiser et al. 2010; Tonry et al. 2012 for further details of the PS1 telescope, observing strategy and data processing). We used PSPHOT, part of the standard PS1 Image Processing Pipeline system (Magnier 2006), to extract point spread function photometry from nightly stacked images of the MDS fields. Each nightly stack is divided into ∼70 skycells. We calibrate each of these separately using Sloan Digital Sky Survey (SDSS) photometry (Fukugita et al. 1996; York et al. 2000) of moderately bright ($16 < \mathrm{mag} < 18.5$) point sources (defined as having type = 6 in the SDSS data base). The bright magnitude cut is used since the brightest objects can create artefacts in the PS1 images. We use 18.5 as the faint cut so that we have a large number of objects used in the calibration of each skycell while ensuring high-precision photometry for each object (95 per cent have errors <0.01 mag).

We found that in some individual cases the flux calibration was unstable due primarily to artefacts around objects used in the flux calibration in the PS1 imaging. To calibrate our data we measure an average offset between the PS1 and SDSS photometry; we also record the rms around this average for each skycell we calibrate. Fig. 7 shows a histogram of the rms of the calibration offset for each epoch of each skycell in the g_{P1} band for the MD03 field. The tail to larger rms is indicative of PS1 skycells that have poor magnitudes for the stars used in the flux calibration. We only accept skycells with rms<0.1 mag. This cut removes ∼5 per cent of the stacked skycells from our sample.

5.2 Hectospectra

Spectra of QSOs in the MDS fields are being taken as part of an ongoing project to study the variability of QSOs. QSO candidates are selected for spectroscopy using current photometric data bases of QSOs based on SDSS photometry (Richards et al. 2009; Bovy et al. 2011) in addition to which point sources that correspond to X-ray sources, variability selected objects and Ultra Violet eXcess (UVX) selected objects are targeted for spectroscopy.

The MDS fields are being surveyed with the Hectospec instrument on the Multiple Mirror Telescope (MMT). Each MDS field is tiled with seven MMT pointings. Exposures are ∼1.5 h in length meaning that an MDS field (∼500 QSOs) can be surveyed in ∼1 night of on-sky observing time.

The spectra are extracted and reduced using standard Hectospec pipelines (Mink et al. 2007). They are then flux calibrated using observations of F stars in the same fields. These stars are compared with a grid of model stellar spectra, created using the spectral synthesis code SPECTRUM (Gray & Corbally 1994; Gray, Graham & Hoyt 2001) with models from Castelli & Kurucz (2004), to correct for the response of the Hectospec instrument. Absolute flux calibration is then made by fitting to the r-band SDSS magnitudes of the stars. Errors in the response correction are typically $\lesssim$10 per cent over the main part of the spectrum (∼4000–8500 Å). However, uncertainty on the absolute flux calibration can have a larger effect on the line fluxes we measure. This depends strongly on the number of stars used in the calibration and is typically $\lesssim$10 per cent. However, in a handful of Hectospec fields some stars are significantly off the average calibration. In general, the spectra of these stars are fainter than expected and may be affected by small positioning errors. These stars are removed manually from the calibration. However, the same problem may affect QSO spectra in our sample.

5.3 Our sample

In total spectra of 855 ($g < 22$) QSOs have been obtained, primarily in MDS fields MD03 and MD07. More information on the selection of this QSO sample and the spectra will be given in an upcoming paper. Further QSO spectra were kindly taken by the MDS transient team. Most QSOs in the sample have only one spectrum and so cannot be used to cross-correlate with the continuum observations. However, 82 of these objects are in the SDSS Data Release 7 QSO catalogue (Schneider et al. 2010). These objects have spectra taken with the Sloan telescope giving us two spectra over a time baseline of ∼10 years (for details of the Sloan spectrograph and SDSS QSO selection see Richards et al. 2002; Stoughton et al. 2002; Gunn et al. 2006). Furthermore, we have taken >1 spectrum of 59 QSOs in our sample giving us a spectroscopic baseline from ∼50 to ∼100 days. In Fig. 8, we show the r_{P1}-band light curve for four QSOs selected from our sample as examples.

5.4 Emission-line fluxes

In Fig. 9 we show the redshift distribution of the 138 QSOs with >1 spectrum. Their distribution is relatively typical of that of the SDSS (and other optically selected) QSO catalogue with the vast majority between $z \sim 0.5$ and 2. This corresponds roughly to the range of redshifts over which the Mg II line is redshifted into optical spectra and we focus on the Mg II line for the rest of this work.

We fit the Mg II line following the prescription outlined in Fine et al. (2008) and each fit is manually inspected to check the reliability. We calculate emission-line flux and error directly from the continuum-subtracted spectrum following Cardiel et al. (1998). The typical S/N of these lines is ∼3–30 for the SDSS spectra and ∼10–200 for the Hectospec spectra. Hence in the case of the Hectospec spectra the error on the line fluxes is dominated by the flux-calibration errors rather than the spectral S/N. The SDSS spectra, that have a flux calibration error of ∼5 per cent (Adelman-McCarthy et al. 2008), are more typically dominated by the statistical noise in the spectra.

Through visual inspection we remove a number of spectra that (i) have broad absorption lines, (ii) have unusual spectra that are poorly characterized by our fitting or (iii) are affected by residual

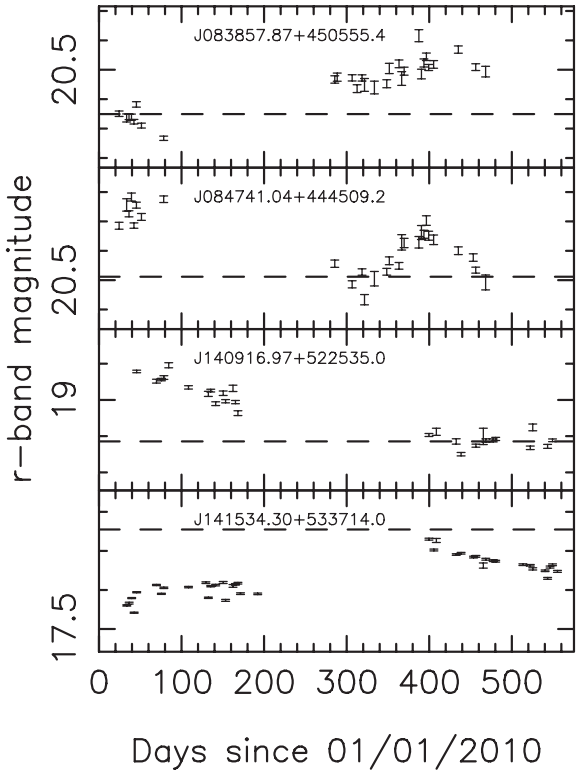

Figure 8. Four example $r_{\rm PI}$-band light curves of QSOs in our sample. The top two and bottom two come from different MDS fields (MD03 and MD07, respectively). All of the objects show evidence for variability over the ∼1 year of monitoring. Dashed lines in each plot indicate the SDSS *r*-band magnitude.

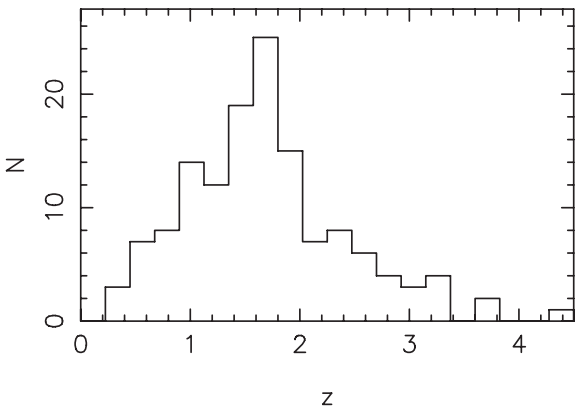

Figure 9. The redshift distribution of the 138 objects that have MDS light curves and >1 spectroscopic observation from the MMT and SDSS. The distribution is typical of optical/UV selected samples and is highly incomplete in the interval $2 \lesssim z \lesssim 3$.

sky/telluric features. In Fig. 10, we show the measured SDSS and Hectospec fluxes for the 42 QSOs that had good Mg II flux measurements from each spectrum. These span nearly two orders of magnitude in luminosity and cover the redshift range $0.45 < z < 1.68$.

5.5 The binned cross-covariance

We calculate the discrete covariance function for the 42 objects with two good Mg II flux measurements. In the calculation we convert the emission-line fluxes to magnitudes, hence we are measuring the fractional (rather than absolute) cross-covariance. We perform the calculation in bins with width 20 days in the rest frame of the observed QSOs. In Fig. 11, we show the covariance function along with the number of data–data pairs in each time-lag bin. The small number of objects and spectra means that there is little signal in the cross-covariance. Furthermore, due to the observing times we have a gap in our time sampling at ∼90 days.

The small number of objects involved means that we were unlikely to find a lag in these data. Fig. 11 is given rather as an example of what can be done with the current data. Note that we do not expect the type of step bias shown in Fig. 2(c) since, in those objects that have spectra from the SDSS, only one of the two spectra is contributing to the correlation function at these lags.

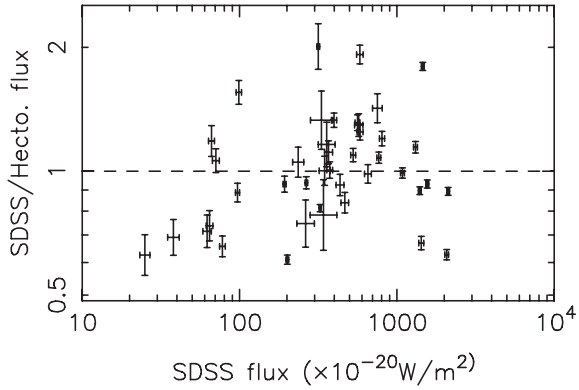

Figure 10. Comparison of the Mg II line flux measured from the archive SDSS spectra and during the Hectospec survey. Errors on the SDSS measurements are dominated by the spectral S/N, while in the Hectospec observations they are dominated by uncertainty in the flux calibration.

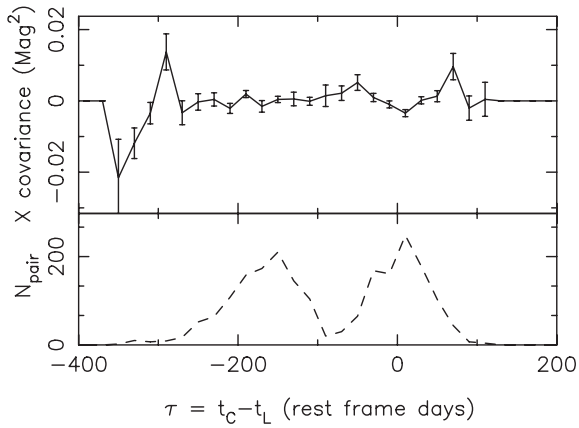

Figure 11. The stacked discrete cross-covariance function for the 42 objects in our final sample. The bottom panel shows the number of emission-line and continuum data–data pairs contributing to each bin. The bins are 20 days (rest frame) in width.

6 SUMMARY

We have demonstrated a technique for stacking cross-correlations and covariances. We focus on QSO emission-line and continuum light curves in the case when only one is well sampled. We demonstrate the technique via a suite of simple simulations that highlight some of its biases and limitations as well as its advantages. While the stacked analyses show smaller peaks and can produce erroneous

steps in the results due to the limited time sampling, the position of the peak remains unbiased. Furthermore, given similar total numbers of emission-line and continuum measurements the technique gives comparable S/N compared to the classic, unstacked approach.

We focus on the Pan-STARRS MDS and show that it may be possible to measure average reverberation lags for QSOs in these fields with a relatively small investment of telescope time based on empirical simulations of QSOs in these fields. Finally, we performed a stacked cross-covariance analysis on 42 QSOs from the MDS that have well-sampled continuum emission and >2 spectra from our observations and the SDSS archive. We find no indication of a peak in these data although the small numbers mean this would have been unlikely. In the near future, multi-epoch spectroscopic observations of MDS fields would be required to allow for stacked lags to be measured.

We note that the same technique could be applied outside of reverberation mapping. The relationship between X-ray and optical variability is complex in QSOs (Shemmer et al. 2003; Marshall, Ryle & Miller 2008; Arévalo et al. 2009) and lags between X-ray and optical light curves can be used to investigate the dominant emission processes at these wavelengths. Here the highly sampled optical data could be combined with wide-field X-ray imaging data (e.g. *XMM*) as an efficient means of producing optical to X-ray cross-correlations. The gain in efficiency would be proportional to the number of X-ray QSOs that can be simultaneously imaged.

ACKNOWLEDGMENTS

The authors would like to acknowledge Peter Draper for assistance in setting up the source extraction software used in this paper. We would also like to thank the MDS transient team for sharing MMT fibres and adding significantly to the size of our QSO sample.

The data in this paper came from the SDSS, Pan-STARRS and the MMT.

Funding for the SDSS and SDSS-II has been provided by the Alfred P. Sloan Foundation, the Participating Institutions, the National Science Foundation, the US Department of Energy, the National Aeronautics and Space Administration, the Japanese Monbukagakusho, the Max Planck Society and the Higher Education Funding Council for England. The SDSS web site is http://www.sdss.org/.

The SDSS is managed by the Astrophysical Research Consortium for the Participating Institutions. The Participating Institutions are the American Museum of Natural History, Astrophysical Institute Potsdam, University of Basel, University of Cambridge, Case Western Reserve University, University of Chicago, Drexel University, Fermilab, the Institute for Advanced Study, the Japan Participation Group, Johns Hopkins University, the Joint Institute for Nuclear Astrophysics, the Kavli Institute for Particle Astrophysics and Cosmology, the Korean Scientist Group, the Chinese Academy of Sciences (LAMOST), Los Alamos National Laboratory, the Max-Planck-Institute for Astronomy (MPIA), the Max-Planck-Institute for Astrophysics (MPA), New Mexico State University, Ohio State University, University of Pittsburgh, University of Portsmouth, Princeton University, the United States Naval Observatory and the University of Washington.

The PS1 surveys have been made possible through contributions of the Institute for Astronomy, the University of Hawaii, the Pan-STARRS Project Office, the Max-Planck Society and its participating institutes, the Max Planck Institute for Astronomy, Heidelberg and the Max Planck Institute for Extraterrestrial Physics, Garching, The Johns Hopkins University, Durham University, the University of Edinburgh, Queen's University Belfast, the Harvard–Smithsonian Center for Astrophysics, and the Las Cumbres Observatory Global Telescope Network, Incorporated, the National Central University of Taiwan and the National Aeronautics and Space Administration under grant no. NNX08AR22G issued through the Planetary Science Division of the NASA Science Mission Directorate.

Observations reported here were obtained at the MMT Observatory, a joint facility of the Smithsonian Institution and the University of Arizona.

REFERENCES

Adelman-McCarthy J. K. et al., 2008, ApJS, 175, 297
Alexander T., 1997, in Maoz D., Sternberg A., Leibowitz E. M., eds, Astrophysics and Space Science Library Vol. 218, Astronomical Time Series. Kluwer, Dordrecht, p. 163
Almaini O. et al., 2000, MNRAS, 315, 325
Arévalo P., Uttley P., Lira P., Breedt E., McHardy I. M., Churazov E., 2009, MNRAS, 397, 2004
Bentz M. C., Peterson B. M., Pogge R. W., Vestergaard M., Onken C. A., 2006, ApJ, 644, 133
Bentz M. C. et al., 2010, ApJ, 716, 993
Blandford R. D., McKee C. F., 1982, ApJ, 255, 419
Bovy J. et al., 2011, ApJ, 729, 141
Cardiel N., Gorgas J., Cenarro J., Gonzalez J. J., 1998, A&AS, 127, 597
Castelli F., Kurucz R. L., 2004, arXiv e-prints
Chelouche D., Daniel E., 2012, ApJ, 747, 62
Cherepashchuk A. M., Lyutyi V. M., 1973, Astrophys. Lett., 13, 165
Croom S. M. et al., 2009, MNRAS, 399, 1755
Denney K. D. et al., 2006, ApJ, 653, 152
Denney K. D. et al., 2010, ApJ, 721, 715
Edelson R. A., Krolik J. H., 1988, ApJ, 333, 646
Fine S. et al., 2008, MNRAS, 390, 1413
Fine S., Croom S. M., Bland-Hawthorn J., Pimbblet K. A., Ross N. P., Schneider D. P., Shanks T., 2010, MNRAS, 409, 591
Fukugita M., Ichikawa T., Gunn J. E., Doi M., Shimasaku K., Schneider D. P., 1996, AJ, 111, 1748
Gaskell C. M., Peterson B. M., 1987, ApJS, 65, 1
Gaskell C. M., Sparke L. S., 1986, ApJ, 305, 175
Gray R. O., Corbally C. J., 1994, AJ, 107, 742
Gray R. O., Graham P. W., Hoyt S. R., 2001, AJ, 121, 2159
Gunn J. E. et al., 2006, AJ, 131, 2332
Haas M. et al., 2011, A&A, 535, A73
Hodapp K. W. et al., 2004, in Oschmann J. M., Jr, ed., Proc. SPIE Vol. 5489, Optical Design of the Pan-STARRS Telescopes. SPIE, Bellingham, p. 667
Horne K., Welsh W. F., Peterson B. M., 1991, ApJ, 367, L5
Kaiser N. et al., 2002, in Tyson J. A., Wolff S., eds, Proc. SPIE Vol. 4836, Pan-STARRS: A Large Synoptic Survey Telescope Array. SPIE, Bellingham, p. 154
Kaiser N. et al., 2010, in Stepp L. M., Gilmozzi R., Hall H. J., eds, Proc. SPIE Vol. 7733, The Pan-STARRS Wide field Optical/NIR Imaging Survey. SPIE, Bellingham, 77330E
Kaspi S., Smith P. S., Netzer H., Maoz D., Jannuzi B. T., Giveon U., 2000, ApJ, 533, 631
Kaspi S., Maoz D., Netzer H., Peterson B. M., Vestergaard M., Jannuzi B. T., 2005, ApJ, 629, 61
Kelly B. C., Bechtold J., Siemiginowska A., 2009, ApJ, 698, 895
MacLeod C. L. et al., 2010, ApJ, 721, 1014
McLure R. J., Jarvis M. J., 2002, MNRAS, 337, 109
Magnier E., 2006, in Ryan S., ed, The Advanced Maui Optical and Space Surveillance Technologies Conference. The Mavi Economic Development Board, Kihei, HI
Marshall K., Ryle W. T., Miller H. R., 2008, ApJ, 677, 880
Mink D. J., Wyatt W. F., Caldwell N., Conroy M. A., Furesz G., Tokarz S. P., 2007, in Shaw R. A., Hill F., Bell D. J., eds, ASP Conf. Ser. Vol. 376,

Astronomical Data Analysis Software and Systems XVI. Astron. Soc. Pac., San Francisco, p. 249
Peterson B. M., 1993, PASP, 105, 247
Peterson B. M., Wandel A., 1999, ApJ, 521, L95
Peterson B. M., Wandel A., 2000, ApJ, 540, L13
Peterson B. M. et al., 2004, ApJ, 613, 682
Richards G. T. et al., 2002, AJ, 123, 2945
Richards G. T. et al., 2009, ApJS, 180, 67
Schneider D. P. et al., 2010, AJ, 139, 2360
Shemmer O., Uttley P., Netzer H., McHardy I. M., 2003, MNRAS, 343, 1341
Stoughton C. et al., 2002, AJ, 123, 485
Tonry J. L. et al., 2012, ApJ, 745, 42
Vanden Berk D. E. et al., 2004, ApJ, 601, 692
Vestergaard M., 2002, ApJ, 571, 733
Wandel A., Peterson B. M., Malkan M. A., 1999, ApJ, 526, 579
Wilhite B. C., Brunner R. J., Schneider D. P., Vanden Berk D. E., 2007, ApJ, 669, 791
York D. G. et al., 2000, AJ, 120, 1579
Zu Y., Kochanek C. S., Peterson B. M., 2011, ApJ, 735, 80
Zu C., Wang Y.-X., Chang X.-Y., Wei Z.-H., Zhang S.-Y., Duan L.-M., 2012, New J. Phys., 14, 033002

This paper has been typeset from a TEX/LATEX file prepared by the author.